Journal of Fluorine Chemistry 290 (2026) 110538

Contents lists available at ScienceDirect

Journal of Fluorine Chemistry

journal homepage: www.elsevier.com/locate/fluor

Surface degradation and modification of traditional Chinese paintings exposed to fluorinated chemical agents

Muying Ge [a], Hongru Zhou [a], Kai Wang [a], Hideki Yoshioka [b], Haiting Wu [a], Ziyi Lu [a], Yafei Zhou [c], Biao Zhou [a,*]

[a] Inner Mongolia Research Institute, China University of Mining and Technology (Beijing), Beijing 100083, China
[b] Department of Architecture, Faculty of Engineering, The University of Tokyo, Tokyo, 113-8654, Japan
[c] China Waterborne Transport Research Institute, Beijing 100088, China

ARTICLE INFO

Keywords:
Fluorinated fire agents
Painting surface
Modification
Corrosion

ABSTRACT

Fires in historic buildings frequently cause severe cultural heritage losses. Fluorinated fire agent can be effectively applied to protect historic buildings. However, fluorinated fire agents may exert certain impacts on the surfaces of artifacts near the fire site. It is essential to elucidate the mechanisms by which fluorinated fire agents affect the surfaces of the interior artworks. This study systematically investigates the surface corrosive and modification effects of five fluorinated fire agents ($C_3H_2BrF_3$, C_9F_{18}, $C_5H_3OF_9$, $C_6F_{12}O$, and $C_3H_2ClF_3$) on the surface of a selected Chinese painting. Colorimetric analysis, SEM, XRD, and FTIR-ATR were used to assess changes in color, microstructural morphology, crystalline composition, and molecular structure, separately. It is found that $C_3H_2BrF_3$ caused severe corrosion to the fiber structure and significantly altered the chemical composition. $C_5H_3OF_9$ induced wrinkling of fibers and disruptions to molecular bonding structures of the painting surface. $C_6F_{12}O$ caused alterations in the crystalline phases and slight structural damage on the surface. $C_3H_2ClF_3$ and C_9F_{18} exhibited comparatively milder effects on surfaces. The findings demonstrate that fluorinated fire agents inflict varying degrees of corrosion and chemical modification on the selected painting surface. It elucidates the surface modification mechanisms induced by fluorinated fire extinguishing agents and contributes to the conservation of cultural heritage.

1. Introduction

Ancient buildings represent a crucial component of historical and cultural heritage, housing a vast collection of ancient calligraphy and paintings that possess profound cultural significance and artistic value. Some historical buildings face high fire risks, due to their unique wooden structure [1,2]. Consequently, the use of fire agents is often unavoidable during fire suppression. Fluorinated-based fire agents have been used in ancient building fires because of their effective fire suppression performance and environmental friendliness. $C_3H_2BrF_3$ (2-bromo-3,3,3-trifluoropropene, CAS No. 1514-82-5), $C_6F_{12}O$ (Perfluoro(2-methyl-3-pentanone), CAS No. 756-13-8), and $C_3H_2ClF_3$ (trans-1-chloro-3,3,3-trifluoropropene, CAS No. 102687-65-0) have been widely used as fire agents. $C_3H_2BrF_3$, $C_6F_{12}O$, and $C_3H_2ClF_3$ exhibit minimum extinguishing concentrations in air of 2.6 %, 4.0 %, and 6.8 %, respectively, demonstrating excellent fire suppression performance [3–6]. In addition, C_9F_{18} (hexafluoropropene trimer, CAS No. 6792-31-0) and $C_5H_3OF_9$ (methoxy-nonafluorobutane, CAS No. 163702-07-6) have shown promising fire suppression potential [7,8]. All of these substances exhibit near-zero ozone depletion potential (ODP) and relatively low global warming potential (GWP) [9–12]. However, existing research has shown that fluorinated fire agents can produce large quantities of corrosive acidic byproducts during fire incident [13,14]. It may cause irreversible damage if acidic byproducts adhere to the surface of ancient calligraphy and paintings. It is of considerable practical significance to systematically investigate the mechanisms and destructive effects of fluorinated fire suppressants on ancient artworks, in order to better protect calligraphy and painting artifacts in historic buildings.

Currently, fluorinated fire agents are widely employed in a variety of applications [15]. Consequently, numerous research have been conducted on fluorinated-based fire agents, including studies on extinguishing concentration [16], fire suppression mechanisms [15], toxicity [17,18], and corrosiveness [19]. Moreover, extensive studies have also

* Corresponding author.
E-mail address: zhoubiao1088@cumtb.edu.cn (B. Zhou).

https://doi.org/10.1016/j.jfluchem.2026.110538
Received 8 November 2025; Received in revised form 17 December 2025; Accepted 9 January 2026
Available online 11 January 2026

been conducted on fires in historic buildings [2,20], including comprehensive reviews of early fire detection and warning technologies [21], as well as investigations into the extinguishing performance of various agents on heritage buildings [22–24]. In the case of fluorinated fire agents, the fluorinated liquid may undergo pyrolysis under extremely high-temperature conditions. This process results in the formation of various pyrolysis products. The properties of the fluorinated liquid after pyrolysis are significantly different from those of the non-pyrolyzed fluorinated liquid. Studies have shown that fluorinated fire agents can produce corrosive acidic substances at elevated temperatures [17,25]. These acidic substances may induce varying degrees of corrosion and discoloration in historic relics [19,26]. However, the impact of fluorinated fire agents on the surfaces of calligraphy and painting artifacts housed within historic buildings remains unclear. To address this research gap and gain a comprehensive understanding of the impact of fluorinated fire agents on cultural heritage, it is essential to systematically investigate the corrosion and modification effects on ancient painting surfaces.

This study aims to preliminarily elucidate the corrosive and modification effects of fluorinated fire agents on the surfaces of traditional Chinese paintings under non-thermal conditions, providing empirical support for the conservation of historical buildings and cultural heritage. Five typical fluorinated fire agents were employed in the present work, including $C_3H_2BrF_3$, C_9F_{18}, $C_5H_3OF_9$, $C_6F_{12}O$, and $C_3H_2ClF_3$. The Chinese painting samples were subjected to a cyclic immersion protocol (once per hour, 5 s per time, repeated 8 times), with independent sampling after each immersion. Subsequently, the sample surfaces underwent colorimetric analysis, scanning electron microscopy (SEM), Fourier-transform infrared spectroscopy with attenuated total reflectance (FTIR-ATR), and X-ray diffraction (XRD) to systematically evaluate their physicochemical variations. The investigation focused on chromatic variation, surface morphological changes, crystalline phase transitions, and molecular structure alterations of the painting surface. The mechanisms by which fluorinated fire agents affect Chinese painting surfaces are elucidated through the combination of the above analytical techniques.

2. Test materials and methods

2.1. Test materials

The experimental material selected for this study was a traditional Chinese painting of lotus flowers, executed on Xuan paper. Traditional Chinese painting pigments were used in the artwork, with the green areas prepared by blending indigo (huaqing) with gamboge (tenghuang). Indigo is a traditional blue mineral pigment, typically extracted from natural lapis lazuli. Gamboge is derived from the extract of the gamboge fruit (Garcinia hanburyi), with its main component being gambogic acid. Prior to the experiment, the Chinese painting was stored for seven days under controlled temperature and humidity conditions (25 ± 2 °C, relative humidity 50 ± 10%) to eliminate the potential influence of environmental factors on material properties. Large areas with uniform coloration were selected for sampling, and specimens were cut into 2 × 2 cm squares, as illustrated in Fig. 1. A colorimeter was used to measure the color coordinates of the sampled regions. The color difference (ΔE*) of the selected samples was controlled to be less than 1.5 to ensure chromatic consistency across all samples [27].

The five fire agents used in the experiments were $C_3H_2BrF_3$ (2-bromo-3,3,3-trifluoropropene, CAS No. 1514-82-5), C_9F_{18} (hexafluoropropene trimer, CAS No. 6792-31-0), $C_5H_3OF_9$ (methoxy-nonafluorobutane, CAS No. 163702-07-6), $C_6F_{12}O$ (perfluoro(2-methyl-3-pentanone), CAS No. 756-13-8), and $C_3H_2ClF_3$ (trans-1-chloro-3,3,3-trifluoropropene, CAS No. 102687-65-0). These chemical agents were purchased from Zhejiang Noah Fluorochemical Co., Ltd., and their physicochemical parameters are summarized in Table 1.

2.2. Test methods

Immersion experiments using a single agent were conducted to better provide a preliminary interpretation of the underlying mechanisms and to avoid the difficulties associated with disentangling multiple coupled factors in real fire scenarios. The Chinese painting samples were subjected to a cyclic immersion protocol (once per hour, 5 s per time, repeated 8 times), with independent sampling after each immersion.

Colorimetric measurements were conducted according to ASTM D2244-89 [28], using a colorimeter (LS171, Linshang Technology, China) to quantitatively analyze the surface color characteristics of the painting samples. Before measurements, the instrument was calibrated with a standard white plate to ensure measurement accuracy. The samples were placed flat on the measurement window, and color coordinate values were measured at five different locations for each sample before and after immersion with fire agents, in order to minimize experimental error. The total color difference (ΔE*) for each treatment group was determined as follows:

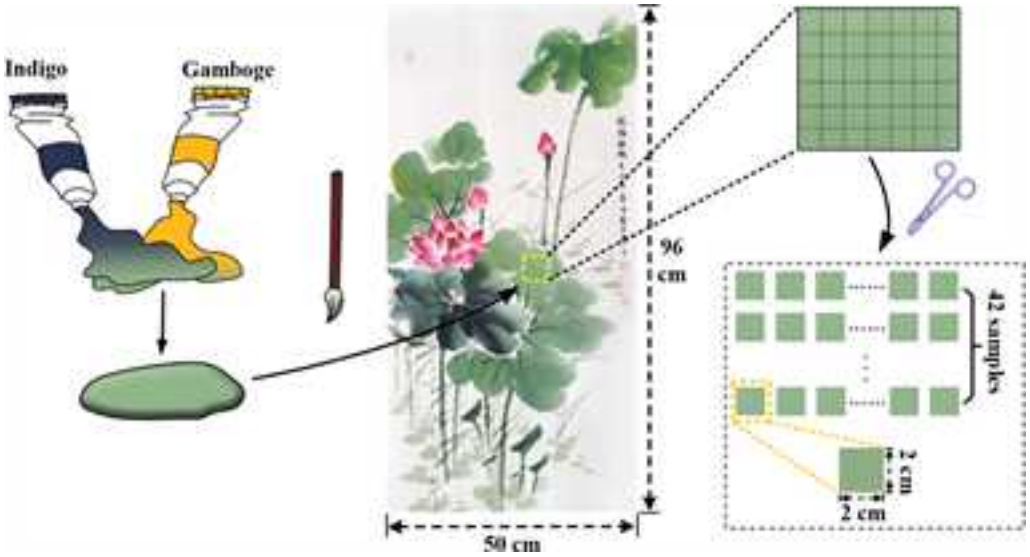

Fig. 1. Sample preparation schematic.

Table 1
Physicochemical parameters of five fire suppression agents.

Chemical Formula	Boiling Point (°C)	Density (g/cm³)	Vapor Pressure (kPa)	Model
$C_3H_2BrF_3$	30	1.69	82 (25°C)	
C_9F_{18}	110	1.83	2.4 (25°C)	
$C_5H_3OF_9$	60	1.53	27 (25°C)	
$C_6F_{12}O$	49	1.60	40.4 (25°C)	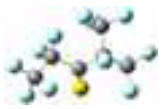
$C_3H_2ClF_3$	19	1.25	129.5 (25°C)	

$$\Delta a^* = a_f^* - a_i^* \quad (1)$$

$$\Delta b^* = b_f^* - b_i^* \quad (2)$$

$$\Delta L^* = L_f^* - L_i^* \quad (3)$$

$$\Delta E^* = \left[(\Delta a^*)^2 + (\Delta b^*)^2 + (\Delta L^*)^2\right]^{\frac{1}{2}} \quad (4)$$

Δa*, Δb*, and ΔL* represent the differences between initial (pre-test) and final (post-treated) values of a*, b* and L*, respectively. An increase in L indicates sample lightening. A positive Δa* denotes a color shift toward red, while a negative Δa* indicates a shift toward green. A positive Δb* signifies a color shift toward yellow, whereas a negative Δb* represents a shift toward blue [26,29].

The microstructural morphology of the samples was characterized using a field emission scanning electron microscope (SEM S-4800, Hitachi, Japan). The samples were evenly mounted onto conductive adhesive tape and fixed onto the sample holder, followed by gold sputter-coating to enhance electrical conductivity. Observations were conducted under magnifications ranging from 600× to 5000×, with the scanning voltage set to 5.0 kV. This enabled a detailed analysis of the surface microstructure, particle size, and particle distribution.

The crystalline structures of the samples were characterized using an X-ray diffractometer (XRD, D8 ADVANCE, BRUKER, Germany). The samples were mounted on the stage and subjected to continuous scanning. By analyzing the position, intensity, and shape of the characteristic diffraction peaks, the phase composition, crystal structure, and lattice parameters of the samples were identified. The obtained patterns were compared with standard PDF cards to determine the crystalline phases present.

The chemical structure of the samples was characterized using Fourier transform infrared spectroscopy with attenuated total reflection (FTIR, Nicolet iS50, Thermo Fisher Scientific, USA). Samples were directly placed on the ATR crystal surface, with sufficient pressure applied to ensure full contact. Scans were performed in the wavenumber range of 4000–400 cm^{-1} with 64 scans and a resolution of 4 cm^{-1}. By analyzing the position, intensity, and shape of infrared absorption peaks, the types of functional groups, as well as chemical structural information, were investigated to infer the molecular structural characteristics of the sample surfaces. The overall experimental procedure is illustrated in Fig. 2.

The macroscopic color changes on the painting surface were examined through colorimetric measurements, while SEM was used to investigate the microscopic alterations in the fiber structure. XRD was employed to study variations in crystal structures and phases after gaining an initial understanding of the macro- and micro-scale changes induced by the extinguishing agents. Finally, FTIR-ATR was used to further characterize the molecular-level changes in functional groups. By integrating analytical techniques across different scales, the effects of fire agents on the painting surface were comprehensively clarified.

3. Results and discussion

3.1. Chromaticity analysis

Colorimetric measurements were conducted on the sample surface after 1 to 8 immersion cycles to determine the macroscopic color changes induced by the fire agents. Five different locations were tested to minimize experimental error for each sample. The L*, a*, b*, and ΔE* values were then analyzed to evaluate the chromatic alterations induced by the five different fire agents on painting surfaces. It is indicated that fire agents affect the surface color of the paintings, which is consistent with findings reported in previous studies [26]. The average L*, a*, and b* values of the untreated samples were 65.0, -7.1, and 12.4, respectively.

As shown in Fig. 3, the mean L* value exhibited a decreasing trend after $C_3H_2BrF_3$ treatment, with the degree of reduction showing a clear positive correlation with the number of immersion cycles. Specifically, the more immersion cycles, the greater the decrease in L*. At eight immersion cycles, the L* value reached its lowest point, with a maximum reduction of 18.1 %, indicating a darkening of the surface. The a* value showed an overall decreasing trend, suggesting that the surface color shifted toward green after $C_3H_2BrF_3$ treatment. The b* value first increased and then decreased. Additionally, visual observation revealed that the surface color changed from light green to dark green following treatment.

As shown in Fig. 4(a), after treatment with $C_5H_3OF_9$, the L* value decreased progressively with increasing immersion cycles. Compared to the untreated group, the a* values decreased to varying degrees after 1-8 immersion cycles, with increases ranging from 13.4 % to 27.0 %, indicating a shift toward green in the surface color following $C_5H_3OF_9$ treatment. The b* value exhibited a fluctuating upward trend. Visually, the surface appeared darker and more yellow.

The Fig. 4(b) shows that the L* value of samples treated with $C_3H_2ClF_3$ remained nearly unchanged. The a* values of samples treated with $C_3H_2ClF_3$ were all lower than those of the untreated group, reflecting a shift toward green, with fluctuations ranging from 2.5 % to 23.1 %. The b* values of the treated samples were consistently lower than those of the control group and decreased progressively with more immersion cycles, ranging from -4.9 % to -37.5 %, indicating a shift toward blue. Visual inspection showed a slight darkening of the surface.

The Fig. 5(a) shows that the L* values of samples treated with C_9F_{18} exhibited slight fluctuations. The a* values showed a decreasing trend, suggesting a color shift toward green after treatment. The value of b* fluctuated slightly around a baseline of 12.4. No significant color change was observed by the naked eye. For samples treated with $C_6F_{12}O$, the L* value showed no significant change, as shown in Fig. 5(b). The decrease in the a* value indicates a shift toward green, with a fluctuation of approximately 10 %. The b* value exhibited slight variations compared with the untreated sample, with no visually discernible color change observed.

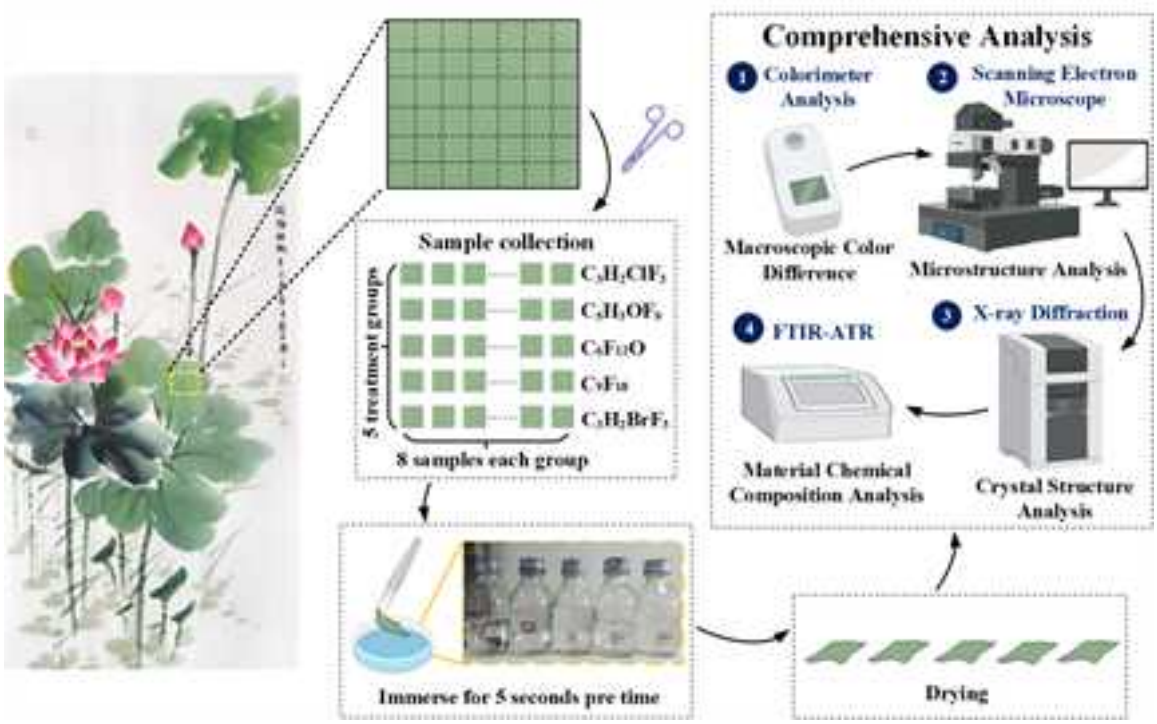

Fig. 2. Experimental setup and procedure.

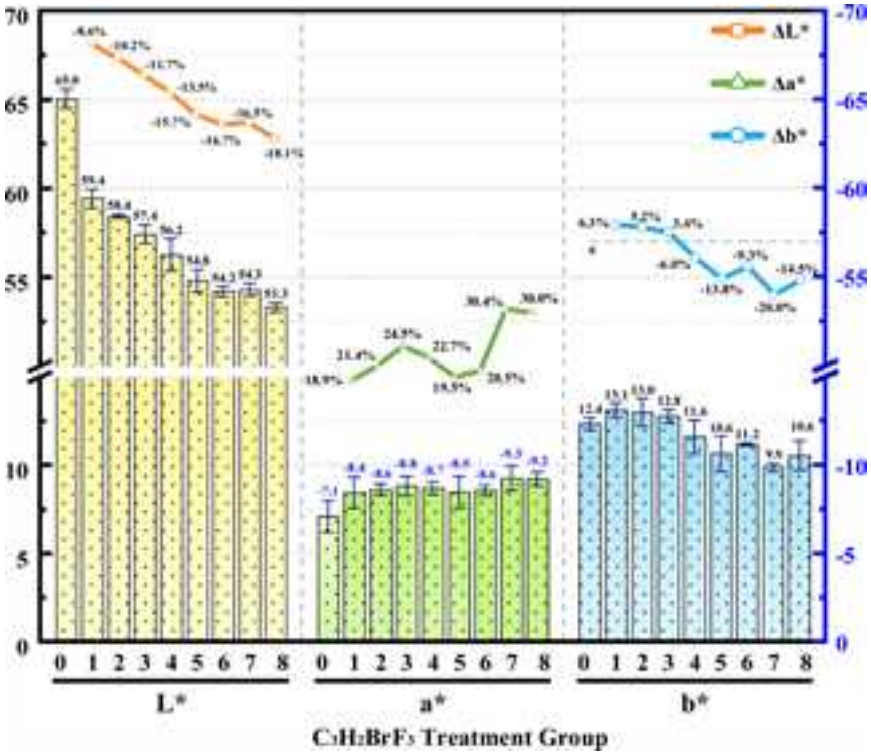

Fig. 3. Color variation in $C_3H_2BrF_3$ treatment group.

Additionally, Fig. 6 shows the ΔE* values after eight immersion cycles. The ΔE* values for the $C_3H_2BrF_3$, $C_5H_3OF_9$, and $C_3H_2ClF_3$ groups increased with more immersion cycles. The largest ΔE* was observed in the $C_3H_2BrF_3$ group, reaching 12.10 after the eighth immersion. This was followed by $C_5H_3OF_9$ and $C_3H_2ClF_3$, with ΔE* values of 7.27 and 4.86, respectively, after the eighth immersion. In contrast, the ΔE* values in the C_9F_{18} and $C_6F_{12}O$ groups remained nearly unchanged. A one-way analysis of variance (ANOVA) was conducted on ΔE*, and values that showed a significant increase in ΔE* were marked with an asterisk (*), as shown in Table 2. This indicates that $C_3H_2BrF_3$ had the most significant impact on color change, while C_9F_{18} and $C_6F_{12}O$ had minimal effect.

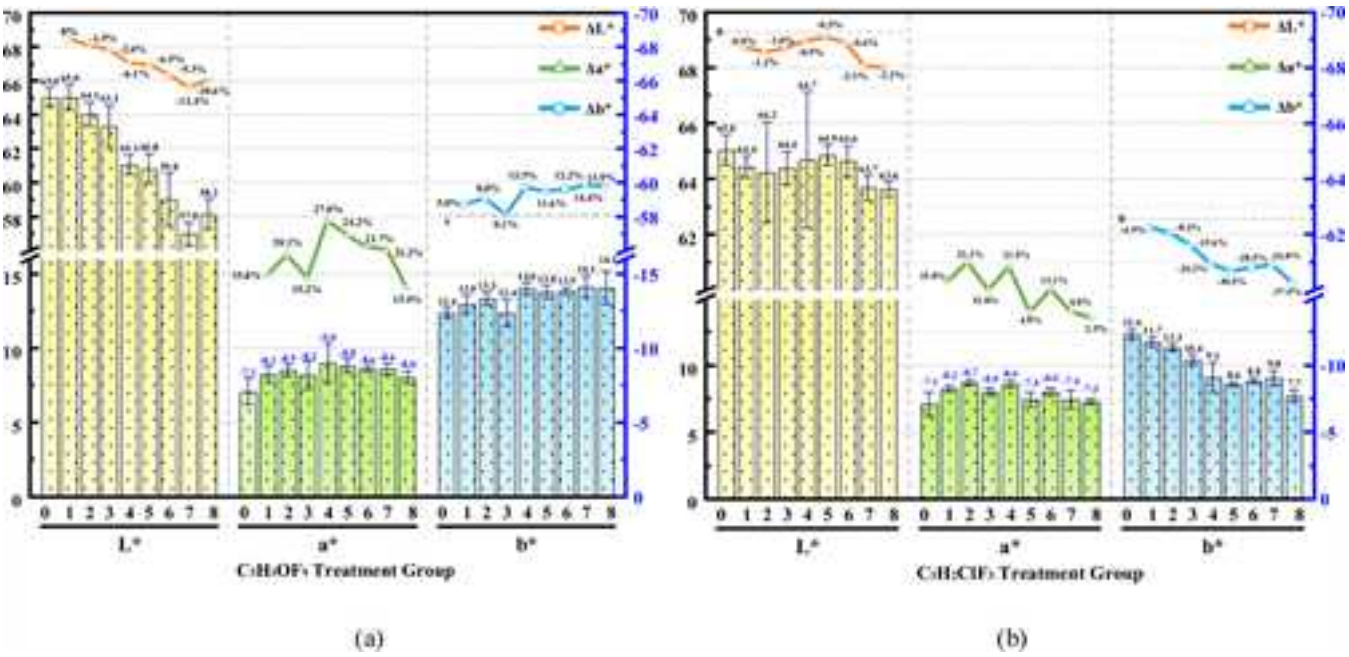

Fig. 4. Color variation analysis. (a) $C_5H_3OF_9$ treatment group (b) $C_3H_2ClF_3$ treatment group.

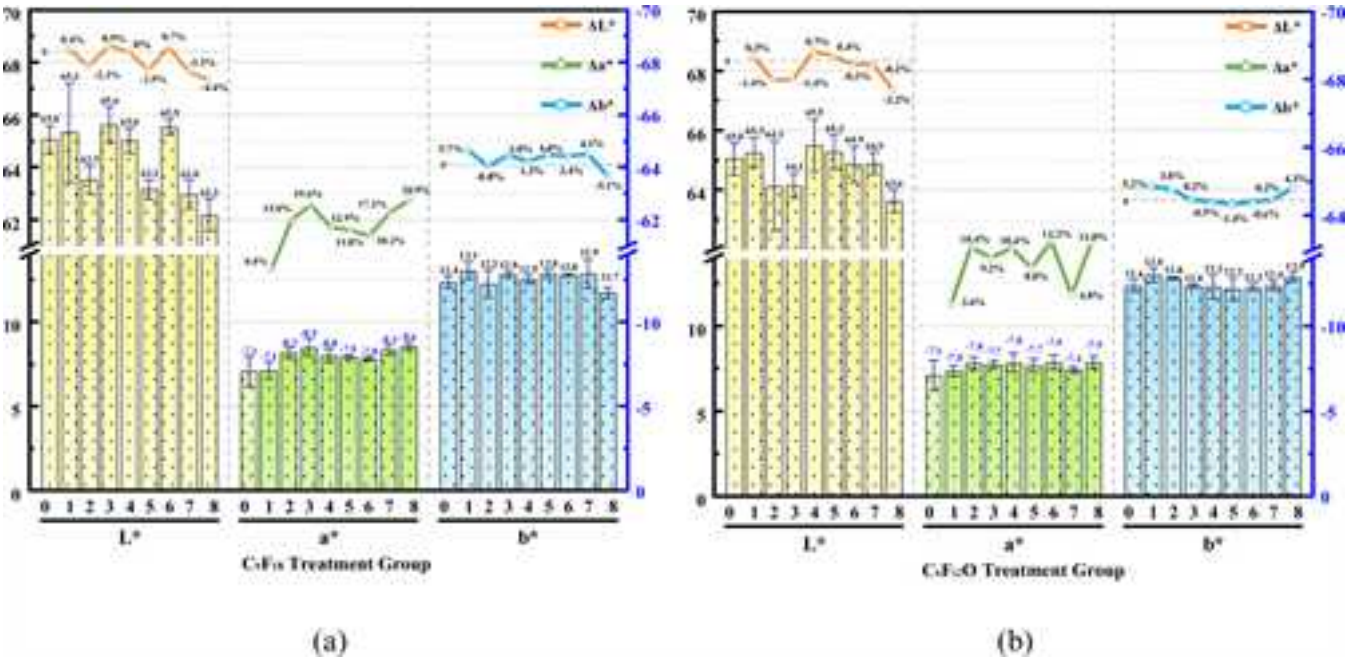

Fig. 5. Color variation analysis. (a) C_9F_{18} treatment group (b) $C_6F_{12}O$ treatment group.

3.2. Microstructural morphology

Scanning electron microscopy (SEM) was employed to observe the surfaces of the traditional Chinese painting before and after 8 times treatment with fluorinated fire agents, in order to investigate the corrosion effects of fire agents on the microstructure of the painting surface.

As shown in the figure, scanning electron microscopy (SEM) images of the Chinese painting surfaces before and after treatment with fire agents are presented. The paper fibers exhibit the characteristic multi-layered structure of natural plant fibers, with well-defined and clearly distinguishable cellulose strands. At higher magnifications, aligned microfibril bundles can be clearly observed on the fiber surface, along with prominent groove-like textures on the cellulose. Amorphous particles of varying sizes are also attached to the surface of the fibers. In the untreated samples, the surface of the paper fibers exhibited a naturally rough texture, with clearly discernible fiber structures and uniformly distributed grooves, as shown in Fig. 7(a) and (b). After treatment with the agents, the cellulose underwent varying degrees of corrosion and morphological changes.

As shown in Fig. 7(c), the cellulose surfaces exhibit noticeable adhesion after treatment with $C_3H_2ClF_3$, which is likely attributed to cellulose swelling or partial dissolution induced by the agent.

In the samples treated with $C_5H_3OF_9$, slight adhesion between

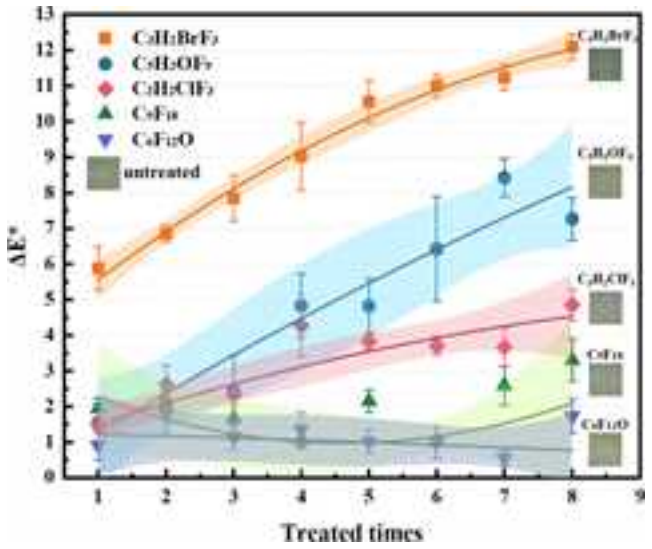

Fig. 6. ΔE* variation with immersion cycles.

cellulose fibers was observed, accompanied by an increase in inter-fiber contact areas and the appearance of pronounced surface wrinkling, as shown in Fig. 7(d) (e). This might primarily be attributed to the low surface tension of $C_5H_3OF_9$ and its interactions with cellulose molecules. The low surface tension of $C_5H_3OF_9$ confers excellent penetration ability, allowing it to rapidly infiltrate the cellulose matrix. This results in surface collapse and shrinkage of the fibers during subsequent evaporation. Its moderate boiling point (61 °C) and vapor pressure ensure that the drying process does not induce excessive damage.

The paper samples treated with $C_6F_{12}O$ exhibited pronounced changes in pore structure compared to the untreated control group, as shown in Fig. 7(f). Pronounced micron-scale pores formed between cellulose fibers in the treated samples, a structural transformation could primarily be attributed to the unique physicochemical properties of $C_6F_{12}O$. Its low boiling point and high vapor pressure promote rapid phase separation during evaporation, thereby exacerbating the dissociation of the fiber network and facilitating pore formation. Unlike solvents $C_3H_2ClF_3$ and $C_5H_3OF_9$, which induce fiber adhesion, treatment with $C_6F_{12}O$ tends to generate an open porous structure.

The samples treated with C_9F_{18} exhibited pronounced structural damage to the cellulose fibers compared to the untreated control group, as shown in Fig. 7(g) (h) (i). Longitudinal tearing and surface delamination of cellulose fibers were observed in the treated samples, indicating a disruption of the fiber network integrity, with localized fiber fracture and stratification. The structural degradation may primarily result from the non-polar nature of C_9F_{18}. When C_9F_{18} infiltrates cellulose, it leads to swelling, negative hornification, and an open structure, consistent with previous studies [30–33]. In contrast to $C_6F_{12}O$, which primarily induces pore formation, C_9F_{18} exhibits significantly greater structural destructiveness on cellulose.

The cellulose materials subjected to $C_3H_2BrF_3$ infiltration exhibited severe structural corrosion, as shown in Fig. 7(j) (k) (l). It displays pronounced fiber adhesion, extensive disruption of the cellulose microfibril network, and the formation of dense fused structures between fibers, indicating a strong dissolving and corrosion effect of $C_3H_2BrF_3$ on the cellulose matrix. Deep groove-like abrasion appeared on the fiber surfaces, and the original ordered microfibril structure was no longer discernible. Particulate matter became embedded within the cellulose surface, with radial cracks emerging around the embedded particles. In addition, XRD analysis revealed the presence of Br and F within the cellulose matrix. It may be attributed to a chemical reaction between $C_3H_2BrF_3$ and cellulose, which disrupted the original fiber structure. Such chemical degradation likely caused the fragmented cellulose to entangle and fuse during solvent evaporation, forming compact adhesive structures. Furthermore, incompatibility between the embedded particles and the cellulose matrix induced interfacial stress, ultimately promoting the propagation of radial microcracks.

In summary, the fire agents induced varying degrees of corrosion to the microscopic structure of the painting surfaces, depending on distinct physicochemical properties. $C_3H_2ClF_3$ caused fiber adhesion, $C_5H_3OF_9$ led to surface wrinkling, $C_6F_{12}O$ promoted porosity, C_9F_{18} induced fiber fracture, and $C_3H_2BrF_3$ produced the most severe degradation and cracking. It is indicated that all five fluorinated fire agents induce varying degrees of corrosion to the microstructure of the surfaces of traditional Chinese painting.

3.3. Crystalline structures

Based on the observed microstructural damage, X-ray diffraction (XRD) analysis was conducted to qualitatively examine the crystalline structures of traditional Chinese painting surfaces before and after 8 times treatment with fluorinated fire agents, in order to reveal the chemical modification effects of different agents on the surface phase composition.

The untreated sample surface primarily consisted of crystalline phases of $CaSO_4$, $CaCO_3$, and $BaSO_4$, which are common inorganic mineral components found in traditional Chinese paintings, as shown in Fig. 8(a). Specifically, $CaCO_3$ is widely used in traditional pigments, $BaSO_4$ is typically present in mineral-based pigments, and $CaSO_4$ may originate from fillers or substrates. After treatment with the fluorinated agents C_9F_{18}, $C_5H_3OF_9$, and $C_3H_2ClF_3$ the surfaces exhibited similar phase transformation behavior: ~~the original SiO_2 phase completely disappeared,~~ new phases of $Ba(OH)_2$ and $Ba(OH)_2(H_2O)_8$ were formed in all treated samples, as shown in Fig. 8(b). It suggests that the treatments induced hydrolysis or structural conversion of barium-containing components, resulting in the formation of $Ba(OH)_2$ species. Moreover, $CaCO_3$ remained detectable in sample surfaces treated with C_9F_{18}, $C_5H_3OF_9$ and $C_3H_2ClF_3$, while the appearance of $CaSO_4$ in the C_9F_{18}-treated sample suggests potential redistribution of calcium species and partial sulfate reconfiguration during the treatment process. In contrast, the sample treated with $C_3H_2BrF_3$ exhibited the emergence of new phases such as BaC_2, $CaO_2(H_2O)_8$, and $Ba(BrF_4)_2$, as shown in Fig. 8(c). It indicates that $C_3H_2BrF_3$ induced more complex chemical reactions and introduced new elements such as F and Br, which reacted with the original inorganic components to form fluorinated and brominated compounds. Similarly, treatment with $C_6F_{12}O$ resulted in the detection

Table 2
Specific ΔE values after 1-8 immersion cycles.

Item	Immersion times							
	1	2	3	4	5	6	7	8
$C_3H_2BrF_3$	5.88±0.61	6.85±0.25*	7.85±0.64*	9.02±0.94*	10.54±0.60*	11.01±0.32*	11.24±0.36*	12.10±0.36*
C_9F_{18}	1.94±0.30	2.05±0.38	1.68±0.61	1.07±0.24	2.15±0.32	1.01±0.09	2.59±0.55*	3.30±0.59*
$C_5H_3OF_9$	1.56±0.52	2.11±0.53	2.43±1.00	4.83±0.90*	4.82±0.77*	6.42±1.46*	8.42±0.54*	7.27±0.60*
$C_6F_{12}O$	0.89±0.39	1.82±0.54*	1.15±0.37	1.36±0.48	1.02±0.33	1.00±0.46	0.55±0.22	1.73±0.49*
$C_3H_2ClF_3$	1.50±0.17	2.63±0.53*	2.32±0.28*	4.27±0.88*	3.83±0.25*	3.71±0.26*	3.67±0.55*	4.86±0.45*

* : Compared with the control group, $P < 0.05$

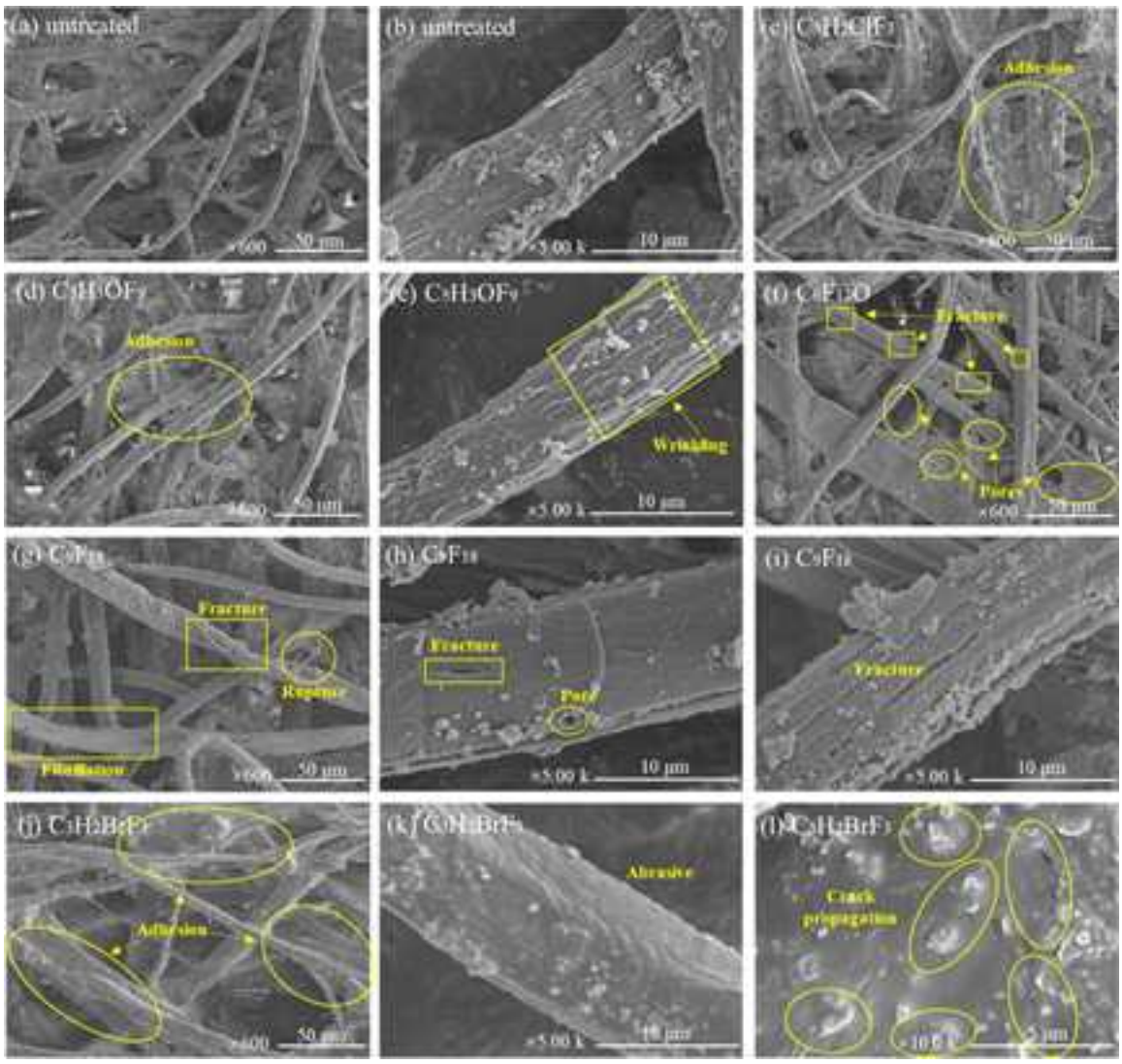

Fig. 7. Microstructural features of cellulose before and after treatment.

of $CaSO_4$, $C_{12}SF_{10}$, $Ca(SO_3)(H_2O)_4$ and $BaSO_4$, indicating the formation of distinct fluorinated reaction products, as shown in Fig. 8(d). It suggests that fluorine from the solvent reacted with sulfate and carbonate species in the sample, leading to phase reorganization.

In summary, the various fluorinated fire agents altered the original mineral phase composition of the painting surfaces to varying degrees, notably inducing the formation of $Ba(OH)_2$ and its hydrates. Additionally, $C_3H_2BrF_3$ and $C_6F_{12}O$ introduced F element more prominently, with $C_3H_2BrF_3$ also introducing Br element, leading to the formation of novel composite compounds. It indicates significant interactions between the fire agents and the painting components, resulting in a certain degree of surface modification.

3.4. Molecular structural characteristics

FTIR-ATR was employed to analyze the surface chemical structure of the samples. The modification impact of the fluorinated fire agents on the molecular structure of the painting surfaces was elucidated, by comparing the molecular structural features of the surfaces before and after 8 times treatment with the agents.

The Fig. 9(a) presents the FTIR-ATR spectra of untreated painting surfaces compared with those treated with $C_3H_2ClF_3$, $C_6F_{12}O$, and C_9F_{18}. It is demonstrated that these three fire agents caused minimal chemical modifications to the painting surfaces. Two prominent characteristic peaks appear at 3335 cm^{-1} and 1650 cm^{-1}, attributable to O-H stretching vibrations and absorbed water, respectively. The peak at approximately 1650 cm^{-1} suggests sample hygroscopicity [34]. The absorption band near 2900 cm^{-1} corresponds to C-H stretching vibrations of methyl groups [35,36]. The signal at 896 cm^{-1}, representing C-O-C stretching vibration, serves as a cellulose crystallinity index [37].

The Fig. 9(b) illustrates the changes in surface functional groups before and after treatment with $C_5H_3OF_9$ and $C_3H_2BrF_3$. After treatment with $C_5H_3OF_9$, a stretching vibration peak of –OH appears near 3332 cm^{-1}, corresponding to the hydroxyl groups in cellulose and bound water on the paper surface. The ether bonds in $C_5H_3OF_9$ interact with the hydroxyl groups to form weak hydrogen bonds, resulting in a shift in vibrational frequency and a redshift of the absorption peak. The stretching vibration peak of C–H observed near 2900 cm^{-1}, attributed to methylene groups in cellulose, shows no significant change before and after treatment. A carbonyl peak appears around 1652 cm^{-1}, corresponding to the stretching vibration of C=O. Its intensity remains largely unchanged due to the absence of functional groups in $C_5H_3OF_9$ capable of forming strong interactions with carbonyls. A new peak appears near 1304 cm^{-1} after treatment, corresponding to the symmetric stretching vibration of $–CF_3$, primarily arising from C–F bonds in perfluoroalkyl groups. The corresponding asymmetric stretching vibration is observed at approximately 1233 cm^{-1}. Asymmetric and symmetric stretching vibrations of $–CF_2–$ appear at around 1211 cm^{-1} and 1136 cm^{-1},

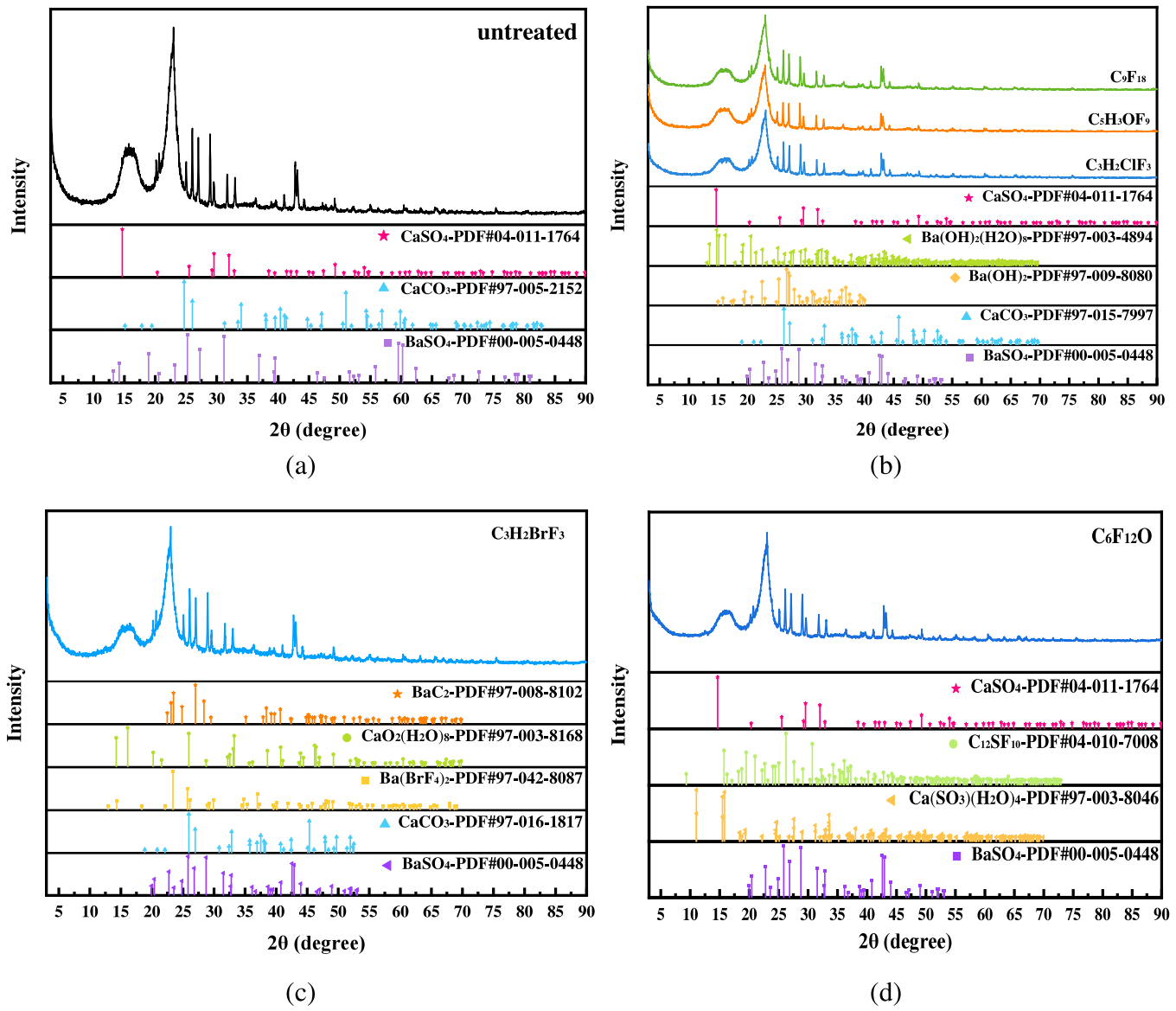

Fig. 8. XRD diffraction patterns of the samples. (a) untreated group (b) C_9F_{18}, $C_5H_3OF_9$, $C_3H_2ClF_3$ treatment group (c) $C_3H_2BrF_3$ treatment group (d) $C_6F_{12}O$ treatment group.

respectively. The collective presence of the peaks confirms the incorporation of $C_5H_3OF_9$ into the sample surfaces. A stretching vibration peak of the C–O–C bond, corresponding to the ether linkage in cellulose, appeared near 1029 cm^{-1}. After treatment, the peak intensity decreased and the peak shape split, which can be attributed to the formation of $–CF_2–O–$ linkages due to the bonding of C–O with $–CF_2$ groups. The structural alteration reduced the bond force constant of the ether bond, thereby restricting its vibrational freedom.

It is revealed that the introduction of $C_5H_3OF_9$ caused a significant shift in the characteristic peaks in the infrared spectrum, confirming that the ether bonds in $C_5H_3OF_9$ molecules disturbed the vibrational environment of the C–O bonds in the surface cellulose of paper through van der Waals interactions. Given that the C–O bond is a key structural unit in the cellulose molecular chain, such interactions essentially led to the deconstruction and degradation of the ~~supramolecularstructure of~~ cellulose. Peaks observed near 795 cm^{-1} and 721 cm^{-1} correspond to the out-of-plane bending vibrations of $–CF_3$ groups, exhibiting a characteristic doublet pattern. The chemical modification induced by $C_3H_2BrF_3$ on the molecular groups of the painting was relatively minor. A C–F stretching vibration appeared near 1060 cm^{-1} in the modified painting, corresponding to the $–CF_3$ structure.

In summary, the fire agents induced varying degrees of modification to the molecular structure of the painting surface. The fire agents $C_3H_2ClF_3$, $C_6F_{12}O$, and C_9F_{18} exerted minimal impact on the surface functional groups of Chinese paintings, whereas $C_3H_2BrF_3$ caused moderate alteration. In contrast, $C_5H_3OF_9$ significantly modified the chemical groups on the painting surface.

4. Conclusion

This study employed cyclic immersion experiments to systematically evaluate the corrosive and modification effects of five representative fluorinated fire agents on a selected traditional Chinese painting surfaces. The main conclusions are summarized as follows:

(1) Regarding color variation: $C_3H_2BrF_3$ induced the greatest color difference, followed by $C_5H_3OF_9$, while $C_3H_2ClF_3$ caused comparatively minor changes. Treatments with C_9F_{18} and $C_6F_{12}O$ resulted in negligible color changes.

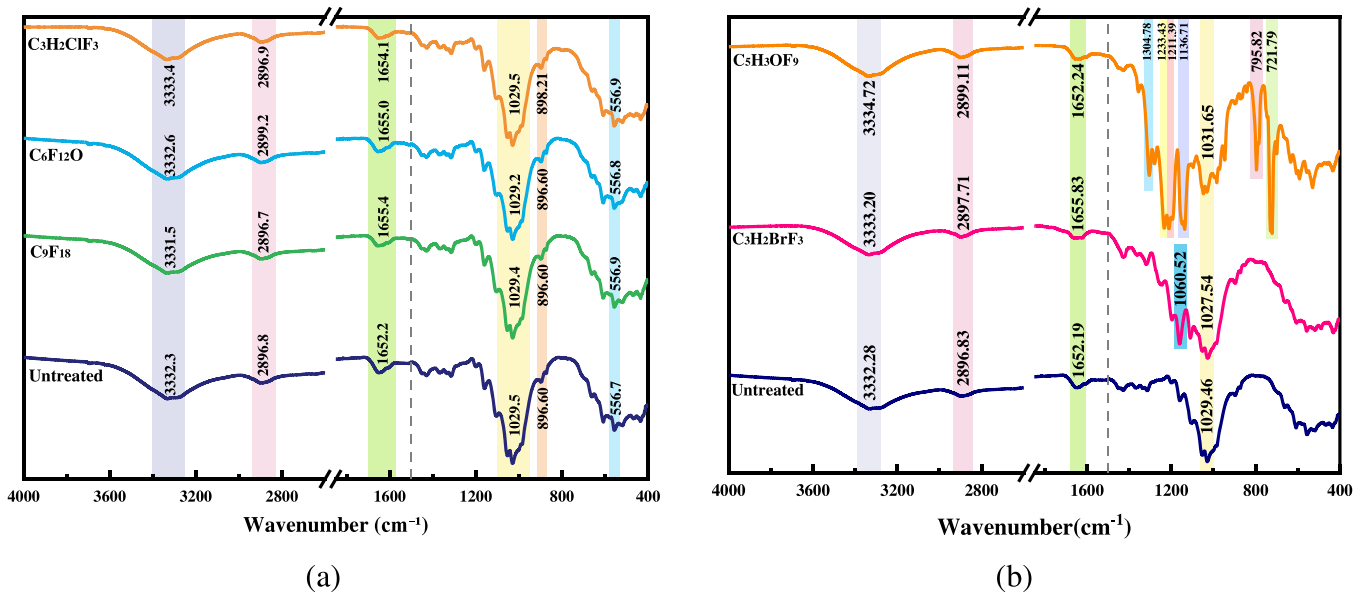

Fig. 9. FTIR-ATR spectra of the samples collected from 4000 to 400 cm^{-1}. (a) $C_3H_2ClF_3$, $C_6F_{12}O$, C_9F_{18} treatment group and untreated group (b) $C_3H_2BrF_3$, $C_5H_3OF_9$ treatment group and untreated group.

(2) Five fluorinated fire agents caused varying degrees of corrosion to the microstructure of the selected Chinese painting surfaces. $C_3H_2BrF_3$ caused severe fiber adhesion and structural collapse, $C_5H_3OF_9$ led to surface wrinkling, $C_3H_2ClF_3$ induced fiber adhesion, C_9F_{18} resulted in fiber cracking, and $C_6F_{12}O$ promoted the formation of porous structures.

(3) Five fluorinated fire agents altered the original mineral composition of inorganic components, regarding crystalline phases, generally promoting the formation of $Ba(OH)_2$ and its hydrates. $C_3H_2BrF_3$ and $C_6F_{12}O$ introduced Br and F elements, resulting in complex new phases, indicative of pronounced chemical restructuring.

(4) FTIR-ATR analysis revealed that the functional group structures of samples treated with $C_3H_2ClF_3$, C_9F_{18}, and $C_6F_{12}O$ remained largely stable. In contrast, $C_5H_3OF_9$ and $C_3H_2BrF_3$ induced significant modification in C–O bond vibrations and the emergence of new absorption peaks, suggesting substantial perturbation of the painting surfaces' molecular structure.

(5) There is a certain urgency in developing next-generation chemical fire suppressants, as current agents pose non-negligible risks of color alteration, microstructural damage, and chemical modification to some cultural relic surfaces.

In summary, the impact of fluorinated fire agents on selected ancient paintings correlates closely with their properties. $C_3H_2BrF_3$ caused the most severe corrosive and modification to the painting surface, with $C_5H_3OF_9$ and $C_3H_2ClF_3$ showing intermediate influence. C_9F_{18} and $C_6F_{12}O$ exhibited relatively mild effects. It offers critical guidance for optimizing fire response strategies in historic buildings. Moreover, it provides methodological references and empirical data to support future studies on the compatibility of conservation materials.

CRediT authorship contribution statement

Muying Ge: Writing – original draft, Investigation, Conceptualization. **Hongru Zhou:** Writing – review & editing, Data curation. **Kai Wang:** Writing – review & editing, Supervision. **Hideki Yoshioka:** Writing – review & editing, Supervision. **Haiting Wu:** Writing – review & editing, Investigation. **Ziyi Lu:** Visualization, Data curation. **Yafei Zhou:** Data curation. **Biao Zhou:** Writing – review & editing, Supervision, Funding acquisition.

Declaration of competing interest

The authors declare that they have no known competing financial interests or personal relationships that could have appeared to influence the work reported in this paper.

Acknowledgements

This work is supported by The Ordos Key Research and Development Program (No. YF20240026), the Beijing Nova Program (No. 202504841008) and The Fundamental Research Funds for the Central Universities (No. 2025ZKPYAQ03).

References

[1] Z. Chen, T. Li, H. Liu, L. Zhang, X. Wen, Fire reconstruction and flame retardant with water mist for double-roofed ancient Buddhist buildings, Buildings 15 (7) (2025) 1109.
[2] J. Li, H. Li, B. Zhou, X. Wang, H. Zhang, Investigation and statistical analysis of fire loads of 83 historic buildings in Beijing, Int. J. Archit. Herit. 14 (3) (2020) 471–482.
[3] V.I. Babushok, G.T. Linteris, D.R. Burgess Jr, P.T. Baker, Hydrocarbon flame inhibition by C3H2F3Br (2-BTP), Combust. Flame 162 (4) (2015) 1104–1112.
[4] K. Wang, D. Ouyang, S. Yuan, D. Wu, J. Zhang, C. Chang, K. Yan, H. Sun, X. Qian, Experimental study on inhibition effect of Novec-1230 on thermal runaway fire of lithium-ion battery packs induced by overcharging, J. Energy Storage 120 (2025) 116451.
[5] R. Wu, X. Wang, L. Cheng, C. Ren, X. Wei, X. Zhang, Experimental and theoretical studies on the thermal decomposition of trans-1-chloro-3,3,3-trifluoropropene and 2-chloro-3,3,3-trifluoropropene and their fire-extinguishing performance, New J. Chem. 44 (30) (2020) 12932–12941.
[6] R. Fan, Y. Pan, X. Shi, Y. Lu, Z. Wang, Investigation on the suppression effect of high momentum C6F12O (Novec-1230) flow on hydrogen jet flame, J. Loss Prev. Process Ind. 84 (2023) 105128.
[7] B. Zhou, M. Ge, K. Wang, H. Yoshioka, J. Han, L. Qin, Z. Tao, W. Wang, T. Chen, Inhibition effect of cooling agent HFE-7100 on lithium-ion batteries (LIBs) thermal runaway in the immersion system, ACS Sustain. Chem. Eng. 13 (24) (2025) 8928–8938.
[8] F. Liu, Q. Hu, C. Jiang, Y. Xu, P. Yan, X. Sui, The suppression performance of fluorinated cooling agents on the lithium-ion batteries fire based on the accelerating rate calorimeter (ARC), Therm. Sci. Eng. Prog. 42 (2023) 101877.
[9] X. Li, Z. Zhou, M. Zhang, F. Zhang, X. Zhou, A liquid cooling technology based on fluorocarbons for lithium-ion battery thermal safety, J. Loss Prev. Process Ind. 78 (2022) 104818.
[10] S.-S. Hsieh, Y.-F. Li, C.-F. Huang, HFE-7100/HFE-7300 spray quenching via a piezoelectric atomizer with a single-hole micronozzle, Appl. Therm. Eng. 175 (2020) 115343.

[11] L. Liu, Z. Du, T. Zhang, Z. Guo, M. He, Z. Liu, The inhibition/promotion effect of C6F12O added to a lithium-ion cell syngas premixed flame, Int. J. Hydrog. Energy 44 (39) (2019) 22282–22300.
[12] G.A. Longo, S. Mancin, G. Righetti, C. Zilio, Boiling of the new low-GWP refrigerants R1234ze(Z) and R1233zd(E) inside a small commercial brazed plate heat exchanger, Int. J. Refrig. 104 (2019) 376–385.
[13] Q. Yang, J. Zhang, Y. Gao, X. Zhou, H. Zhang, Toward better halon substitutes: effects of H content on pyrolytic and fire-suppressing mechanisms of ozone-friendly fluorinated alkanes, J. Mol. Struct. 1285 (2023) 135506.
[14] A. Kim, G. Crampton, Corrosion of electronic components by hydrogen fluoride, J. Fire Prot. Eng. 18 (1) (2008) 55–73.
[15] Q. Yang, Y. Gao, Y. Yang, X. Zhou, H. Zhang, Toward better halon substitutes: effects of carbon chain length on pyrolytic and fire-suppressing mechanisms of perfluoroalkanes, J. Mol. Struct. 1312 (2024) 138589.
[16] X. Wang, R. Wu, L. Cheng, X. Zhang, X. Zhou, Suppression of propane cup-burner flame with HFO-1336mzz(Z) and its thermal stability study, Thermochim. Acta 683 (2020) 178463.
[17] X. Meng, L. Jiang, Q. Duan, S. Wang, P. Duan, Z. Wei, L. Zhang, Z. Jia, K. Jin, Q. Wang, Experimental study on exploration of optimum extinguishing agent for 243 ah lithium iron phosphate battery fires, Process Saf. Environ. Prot. 177 (2023) 138–151.
[18] Y.T. Zhou, P.J. Zhang, S.P. Wang, C.H. Li, J.Q. Zhang, W.X. Zhang, Y.D. Zhao, Y. C. Cao, J.X. Fan, Biosafety assessments of hexafluoropropylene trimer derivative as a fluorinated cooling fluid for electronics, Toxicol. Res. 40 (3) (2024) 431–440.
[19] H. Xing, S. Lu, H. Yang, H. Zhang, Review on research progress of C6F12O as a fire extinguishing agent, Fire 5 (2) (2022) 50.
[20] Z. Biao, Z. Xiao-meng, C. Ming-yong, Fire protection of historic buildings: A case study of group-living Yard in Tianjin, J. Cult. Herit. 13 (4) (2012) 389–396.
[21] B. Zhou, C. Jiang, K. Wang, X. Romão, H. Yoshioka, W. Wang, Z. Tao, H. Zhao, A review: the analysis of fires in Chinese historic building and research progress on the fire protection, Therm. Sci. Eng. Prog. 54 (2024) 102850.
[22] Z. Xiaomeng, Z. Biao, J. Xiang, Study of fire-extinguishing performance of portable water-mist fire extinguisher in historical buildings, J. Cult. Herit. 11 (4) (2010) 392–397.
[23] B. Zhou, J. Sun, X. Sun, K. Wang, C. Qingqing, X. Wang, Y. Han, The effects of hydrogen fluoride on the wooden surface of historic buildings during fire suppression using fluorinated chemical gases, Int. J. Archit. Herit. 17 (4) (2023) 604–614.
[24] M. Benfer, E. Williams, Assessing the impact of fire extinguisher agents on cultural resource materials, Fire Technol. 54 (1) (2018) 289–311.
[25] J. Zhang, W. Gao, L. Chen, Y. Li, Inhibition and enhancement of hydrogen explosion by perfluorohexanone, Int. J. Hydrog. Energy 53 (2024) 522–534.
[26] W. Ke, W. Yang, B. Zhou, K. Wang, J. Sun, X. Sun, M. Xu, Q. Chen, B. Qiu, W. Wang, The color change analysis of historic wooden remains after fire-suppression by fluorinated chemical gases, Herit. Sci. 9 (1) (2021) 93.
[27] R. Ghinea, M.M. Pérez, L.J. Herrera, M.J. Rivas, A. Yebra, R.D. Paravina, Color difference thresholds in dental ceramics, J. Dent. 38 (2010) e57–e64.
[28] F.W. Billmeyer Jr, H.K. Hammond III, ASTM standards on color-difference measurements, Color Res. Appl. 15 (4) (1990) 206–209.
[29] J.S. Fabiyi, A.G. McDonald, M.P. Wolcott, P.R. Griffiths, Wood plastic composites weathering: visual appearance and chemical changes, Polym. degrad. stab. 93 (8) (2008) 1405–1414.
[30] M. Hashemzehi, B. Sjöstrand, H. Håkansson, G. Henriksson, Degrees of hornification in softwood and hardwood kraft pulp during drying from different solvents, Cellulose 31 (3) (2024) 1813–1825.
[31] M.Le Gars, P. Roger, N. Belgacem, J. Bras, Role of solvent exchange in dispersion of cellulose nanocrystals and their esterification using fatty acids as solvents, Cellulose 27 (8) (2020) 4319–4336.
[32] S. Cichosz, K. Dems-Rudnicka, M. Łapiński, A. Jastrzębska, A. Masek, Statistical evaluation of the changes in cellulose properties caused by the stepwise solvent exchange and esterification, Ind. Crops Prod. 203 (2023) 117118.
[33] M. Norgren, C. Costa, L. Alves, A. Eivazi, C. Dahlström, I. Svanedal, H. Edlund, B. Medronho, Perspectives on the Lindman hypothesis and cellulose interactions, Molecules 28 (10) (2023) 4216.
[34] J. Ferreira-Villadiego, J. Garcia-Echeverri, M. Vidal, J. Pasqualino, P. Meza-Castellar, H. Lambis-Miranda, Chemical modification and characterization of starch derived from plantain (Musa paradisiaca) peel waste, as a source of biodegradable material, Chem Eng Trans 65 (2018).
[35] R. Kizil, J. Irudayaraj, K. Seetharaman, Characterization of irradiated starches by using FT-Raman and FTIR spectroscopy, J. Agric. Food Chem. 50 (14) (2002) 3912–3918.
[36] C. Liang, R. Marchessault, Infrared spectra of crystalline polysaccharides. I. Hydrogen bonds in native celluloses, J. Polym. Sci. 37 (132) (1959) 385–395.
[37] K.-H. Teng, M.-H. Lee, PEDOT: PSS treated Xuan paper as a green electronics material for wearable dry electrocardiogram electrodes and flexible strain sensors, J. Environ. Chem. Eng. 13 (2) (2025) 115716.